Co-funded by the

CEBAMA

➢ (Contract Number: 662147)

Deliverable D 1.07

Manuscript for peer-reviewed publication on results generated in WP1

Authors: Tapio Vehmas, Vanessa Montoya, Maria Cruz Alonso, Radek Vašíček, Emily Rastrick, Stephane Gaboreau, Petr Večerník, Markku Leivo, Erika Holt, Naila Ait Mouheb, Jiří Svoboda , David Read, Radek Červinka, Rita Vasconcelos, Claire Corkhill

Date of issue of this report: 4.7.2019

Report number of pages: 20

Project co-funded by the European Commission under the Euratom Research and Training Programme on Nuclear Energy within the Horizon 2020 Framework Programme		
Dissemination Level		
PU	Public	X
PP	Restricted to other programme participants (including the Commission Services)	
RE	Restricted to a group specified by the partners of the CEBAMA project	
CO	Confidential, only for partners of the CEBAMA project	

Start date of project: 01/06/2015 Duration: 48 Months

Manuscript for CEBAMA reference concrete and paste studies,
submitted July 4 2019 to journal of Applied Geochemistry, special edition.

Low-pH Cementitious Materials containing Slag used in Underground Radioactive Waste Repositories

Tapio Vehmas*[1],Vanessa Montoya[2], Maria Cruz Alonso[3], Radek Vašíček[4], Emily Rastrick[5], Stephane Gaboreau[6], Petr Večerník[7], Markku Leivo[1], Erika Holt[1], Naila Ait Mouheb[2], Jiří Svoboda[4] , David Read[5], Radek Červinka[7], Rita Vasconcelos[8], Claire Corkhill[8]

[1]VTT Technical Research Centre of Finland, Espoo, Finland

[2] Institute for Nuclear Waste Disposal (INE), Karlsruhe Institute of Technology (KIT), 76021, Karlsruhe, Germany

[3] CSIC Institute of Construction Science Eduardo, Spain

[4] Faculty of Civil Engineering, Czech Technical University in Prague, Czech Republic

[5] University of Surrey, United Kingdom = 2 authors, double affiliation

[6] The French Geological Survey (BRGM), France

[7] ÚJV Řež, a. s., Czech Republic

[8] NucleUS Immobilisation Science Laboratory, Department of Materials Science and Engineering, University of Sheffield

*tapio.vehmas@vtt.fi, VTT Technical Research Centre of Finland, Kemistintie 3, Espoo, P.O. Box 1000, FI-02044 VTT, Finland

ABSTRACT

Cementitious materials are used for structural and isolation purposes in radioactive and nuclear waste repositories. For example, concrete is used for deposition tunnel end plugs, grouts for rock bolting and injection grouts for fissure sealing. Cementitious materials may or may not form part of engineered barrier systems, which isolate the waste from the biosphere. In the latter case, the properties of the engineered barrier system should not be significantly impaired by the presence of cementitious materials. A cementitious mix design having a suitable composition with respect to an engineered barrier system was developed by blending traditional cements with high amounts of supplementary cementitious materials. Blast furnace slag has a high degree of homogeneity and is likely to be available during the construction period of a repository, an important consideration given the long timescales involved. In the EU-funded project Cebama, a slag-based mix design was developed and analysed by multiple laboratories. Results were compared to traditional concrete and other repository compatible alternative mix designs. According to the results, the mix design was similar to other repository compatible mix designs. Pore solution pH of the matured samples was between 11.4 - 11.6. The pH of cementitious leachates varied between 8.1-11.75, depending on groundwater composition, temperature and experimental set-up. Porosity of the developed concrete was low. Total porosity was under 13% and less than 4% of the porosity was measurable with mercury intrusion porosimetry. Compressive strength of the concrete was 115 MPa, corresponding to traditional high-performance concrete.

KEYWORDS: Low-pH cement, Blast furnace slag, Nuclear Waste, concrete, mortar

1. INTRODUCTION

Nuclear power generation is a viable solution for decreasing CO_2 emissions and mitigating climate change at an intermediate time scale. However, a major disadvantage is production of nuclear waste in various forms and levels of radioactivity. The management and disposal of high-level waste (HLW) consisting of chemically processed and vitrified spent nuclear fuel or spent fuel itself will become a major task. Although the volume of HLW is small, compared to the total volume of nuclear waste generated, it contains 95% of the total radioactive inventory[1].

Deep underground repositories are the most likely option for final disposal of HLW in many countries. Depending on the selected repository site, final disposal concepts will vary to suit local conditions. According to current plans, the first operational repositories will be in the Nordic countries and emplaced in crystalline bedrock[2]. Clay-rock repositories are also a widely studied option, which will shortly follow crystalline-rock repositories[3].

In deep underground repositories, HLW is disposed of in bedrock hundreds of metres below the surface, which naturally isolates the waste from the biosphere. The safety of the repository is ensured via a combination of natural and engineered barriers. The former consists of the surrounding bedrock and its inherent isolating properties. In the case of repositories in crystalline rocks, the engineered barrier system comprises water- and gas-tight sealed copper canisters with a cast iron insert and bentonite-based buffer and backfill[4]. Bentonite has an important role in crystalline rock repositories, protecting the canister from small bedrock movements and potentially adsorbing any radionuclides released from the primary containment. Additionally, bentonite inhibits groundwater movement into the repository and is intended to return the disposal environment to one close to natural conditions due to wetting-induced swelling[4] [5].

Concrete and other cementitious materials are used significantly in repositories for structural support and isolation purposes. For example, concrete plugs are used for sealing the repository and the deposition tunnels whilst also ensuring mechanical and hydrological isolation of various repository compartments. In addition to concrete plugs, cementitious materials are used in shotcrete for tunnel wall rock supports, rock-bolting grouts and injection grouts for fissure sealing.

In order to meet performance requirements during the lifetime of the repository, it is important that the properties of the engineered barrier system should not be impaired by the presence of cementitious materials. Nevertheless, groundwater, backfill and closure materials will be in direct contact with cementitious materials. It has been assumed that cementitious leachates will interact with the host rock, backfill and closure materials but not to an extent that compromises the long-term safety of the barrier system. Migration of these leachates may also affect the bentonite buffer, despite not being in direct contact with cementitious materials [5].

Cementitious mix designs having a more suitable composition with respect to bentonite stability have been formulated [6]–[15]. Mechanical properties and durability are usually considered to be similar to ordinary Portland cement-based formulations, although some disagreements remain [16]. These “low-pH” formulations consist of low alkaline Portland cements mixed with large amounts of supplementary pozzolanic materials, which react with the hydration products that control the pH and composition of cement pore solutions. Consequently, these mix designs are still highly basic but the pH value is significantly lower than in traditional Portland cements. ”low-pH” mix designs usually consist of binary or ternary blends with silica fume and fly ash as the most commonly used supplementary materials. One example is the successful casting of a massive tunnel end plug with a ternary blended cement that has been demonstrated by Posiva Oy in the DOPAS project on plugs and seals [17], [18]. In this case, the ”low-pH” concrete consisted of a ternary blend with low-alkali ordinary Portland cement, granulated silica fume and low-calcium fly ash. Although fly ash has been demonstrated to be a good option for “low-pH” mix designs, it also has its drawbacks. For example,

fly ash is a by-product of energy generation from combustion of fossil coal. As combustion of fossil coal is likely to reduce over the next few years, fly ash might not remain available throughout the construction and operational periods of a repository. These timescales will exceed the operational lifetime of nuclear power plants by decades; therefore, fly ash availability should be evaluated within a hundred-year time span. Even if fly ash remains available throughout the repository construction period, it is expected that quality may decrease owing to the use of alternative fuel resources. The homogeneity of fly ash is already a problem, which will likely increase in the future. In spite of the drawbacks, the benefits of fly ash are that it has a low water demand, is relatively inexpensive and has a high amorphous silica content [19].

Slag-based "low-pH" mix designs have not been studied to the same extent as their fly ash and silica counterparts. Blast furnace slag is an industrial by-product of iron and steel production with the advantage that it has substantially greater homogeneity than fly ash due to production requirements. Due to the nature of its production, blast furnace slag is likely available throughout the anticipated repository construction period. It is also a source of calcium but without the excessive heat of traditional Portland cement, limiting temperature development in massive structures.

For the above reasons, the main focus of the current study is to design and characterise a slag-based ternary mix and compare its performance to binary and ternary blends of silica fume and fly ash based materials. The results were also compared to traditional concrete to better understand the performance of "low-pH" mix designs. The mix used is a slag-based alternative for a ternary mix design that has been successfully used in repository castings [18], [20]. The major components, calcium/silica -ratio, binder content and water/binder -ratio were the same as those of the silica and fly ash based ternary blends [20].

In addition to concrete, a micro-mortar version of the mix design was also studied. The micro-mortar version provides more detailed information on the binder phase and can be considered as an aggregate-free concrete. Mechanical, chemical, microstructural and hydraulic characterisation was performed in various laboratories within the frame of the EU-funded project Cebama [21]. The materials studied also served as an internal reference for the Cebama project and enabled comparison between the experimental protocols used in different laboratories (i.e leaching, percolation experiments) and as input parameters for the modelling work performed within the project [22].

2. MATERIALS

The mix designs for the concrete and micro-mortar are presented in Table 1. The ordinary Portland cement (OPC) used was low-alkali, medium heat ordinary Portland cement LA MH CEM I 42.5 from Cementa Ab (Annläggninscement Degerhamn). Granulated silica fume (SF) and blast furnace slag (BFS) were from Finnsementti Oy (Parmix silika and Masuunikuona KJ400). Elemental compositions of the binder materials were determined by X-ray fluorescence (XRF) and are presented in Table 2. The superplasticizer for achieving the target workability was a naphthalene sulfonate (Pantarhit LK FM from Ha-Be Betonchemie GmbH). The aggregate was a local granitic material of Finnish origin from Rudus Oy. The particle size distribution of aggregates is presented in Table 1. Quartz filler was from Sibelco Nordic Oy (Nilsiä). A description of the batching procedure and more details of the mix design and materials are available elsewhere [23].

A low-density version of the concrete was additionally manufactured for the percolation studies, which included air-entrainment to increase porosity. Low-density samples contained 0.12% (from binder weight) air entrainment agent (Microair from Finnsementti) and water/binder-ratio of 0.6. The air content of the low-density concrete was 2.7% and the density of the samples was 2320 kg/m^3.

Table 1. *Mix designs of studied "low-pH" concrete and micro-mortar.*

Materials	Concrete [kg/m^3]	Micro-mortar [kg/m^3]
CEM I 42.5	105	468
Silica fume	110	491
Blast furnace slag	65	290
Quartz filler*	116	517
0-1mm	168	-
0-8mm	770	-
8-16mm	532	-
16-32mm	396	-
Water (effective)	120	312
Superplasticizer	16.8	75
Water/binder -ratio	0.43	0.25

***Particle size distribution: (70% < 63 µm and 30% between 63- 250 µm)*

Table 2. *Oxide composition of the binder materials (wt. %)*

Binder	CaO	SiO_2	Al_2O_3	SO_3	MgO	Fe_2O_3	K_2O	Na_2O	CO_2	TiO_2	MnO	SrO	ZrO_2
SF	1.46	93.1	1.44	0.47	0.88	0.91	1.73	-	*n.d.*	-	-	-	-
OPC	66.2	17.9	3.52	3.92	0.68	5.17	0.645	0.08	1.32	0.23	0.25	0.03	0.01
BFS	42.3	32.6	10.23	2.54	7.86	0.78	0.61	0.62	*n.d*	1.70	0.38	0.05	0.03

n.d = not determined

Different groundwater and porewater compositions have been used in the leaching, diffusion, compressive strength evolution measurements and percolation experiments (see section 3). Groundwater compositions are presented in Table 3. The bentonite containing solution was labelled as B75. Detailed information on the groundwater origin and compositions are available in [24].

Table 3. *Groundwater and porewater composition (mg/l), used in the methods described in the section 3.*

[mg/l]	Granitic I	Granitic II	Granitic III	Clay I	Clay II	Saline	Bentonite*
Na	63.2	0.4	18.1	1118.1	130.0	3035.9	5773
K	4.1	0.0	2.0	52.6	0.7	104.7	73.6
Mg	4.7	0.0	3.9	153.7	8.9	8.2	230
Ca	16.2	0.2	86.8	241.4	11.0	682.3	596
Sr	-	-	-	-	-	-	9.1
Al	-	-		-	-	-	0.01200
Fe	-	-		-	-	-	$0.8x10^{-3}$
Cl	75.2	0.0	14.6	1901.5	24.0	6246.9	8271.5
Br	-	-	-	-		-	-
SO_4	7.4	0.1	105.7	1434.8	76.0	470.1	694.8
Si	-	-	-	-	-	-	2.1
HCO_3^-	-	0.4	206.4	-	3.2	-	12.3
pH	8.1	9.7	7.7	6.3	8.0	7.6	8.0

**artificial porewater prepared inside an argon (Ar) glove-box according to the water composition provided by Bradbury and Baeyens* [25]*. Different amounts of solids (20.18 g NaCl, 0.23 g KCl, 3.04 g $MgCl_2$ 6H_2O, 0.857 g $MgSO_4$ 7H2O, 0.06 g $SrCl_2$ 6H_2O, 0.094 g Na_2CO_3, 19.89 g Na_2SO_4, 4.11 g $CaCl_2$ 2H_2O, 10.01 g $CaCO_3$) were dissolved in 2 L ultrapure water (MilliQ system, Millipore) in a PE bottle. Additionally, 60 µL of a solution of 6.16 M Na_2Si and 16 mL of sulfuric acid H_2SO_4 (0.04 M) were added to adjust the silicon content and the pH of the solution, respectively.*

3. METHODS

3.1 Characterization of the micro-mortar

Workability was measured using the Haegermann method according to DIN 1164. Air content, compressive strength and density were determined according to SFS standards (SFS-EN 12350-2, SFS-EN 12350-7, EN 12390-3 and EN12390-9). Additionally, the compressive strength evolution was determined using a non-standard compressive punch test [26][27][28]. Punch test samples were exposed to various groundwater compositions in order to evaluate groundwater influence on mechanical properties. The stiffness was derived from the linear section of particular strength test.

The chemical and structural properties were determined by using different complementary techniques. Initially, 5 mm of sample was removed from the surface to obtain regions unaffected by atmospheric carbon dioxide. For analysis by X-Ray Diffraction (XRD), thermogravimetric analysis / differential scanning calorimetry (TG-DSC) and ^{29}Si and ^{27}Al Magic angle spinning nuclear magnetic resonance (^{29}Si and ^{27}Al MAS NMR), samples were crushed and powdered in a grinder for 2 minutes. Ground samples were immersed in isopropanol for 15 minutes, then filtered using a Buchner funnel. The samples were dried in a compartment dryer at 40°C for 10 min to ensure elimination of isopropanol. For X-ray absorption spectroscopic measurements, pellets were pressed after mixing powdered samples with boron nitride.

Scanning electron microscopy - energy dispersive X-ray spectroscopy (SEM-EDX) measurements were performed using an ESEM (model FEI Quanta 650 FEG), equipped with an EDX spectrometer (model Thermo Scientific NORAN System 7) for elemental microanalysis. XRD analysis was performed with a Bruker D8 ADVANCE diffractometer using Cu Kα radiation under controlled N_2 atmosphere. TG-DSC was conducted using a heating rate of 10°C/min from 25 to 1200 °C with a STA409 (Netzsch Gerätebau GmbH) under N_2 atmosphere. The ^{29}Si and ^{27}Al MAS NMR spectra were acquired with Bruker Avance III 400 wide-bore spectrometer with a magnetic field strength of 9.4 T at 104.28 MHz for ^{27}Al and 79.50 MHz for ^{29}Si. Free induction decay was recorded with only 8k-16k data points. The observed ^{29}Si resonances were analysed

using the Q_n(mAl) classification, where a Si tetrahedron is connected to n Si tetrahedral with n varying from 0 to 4 and m is the number of neighbouring AlO_4 tetrahedra.

Information on iron and chlorine speciation was obtained by probing their K-edge by X-ray absorption spectroscopy (XAS). Fe K-edge XAS data were recorded at the BM26A beamline[29] at the European Synchrotron Radiation Facility (ESRF, Grenoble, France). Fe K-edge spectra for powdered micro-mortar, concrete and reference compounds were recorded either in transmission or in fluorescence detection mode using a 9 element monolithic Ge fluorescence detector. Selected reference compounds are C2F ($Ca_2Fe_2O_5$), C4AF ($Ca_2(Fe,Al)_2O_5$), the starting clinker, hematite (α-Fe_2O_3), ferrihydrite, silica fume, C-S-H phases and ferric sulfate ($Fe_2(SO_4)_3.xH_2O$).The Fe K-edge spectrum of goethite was recorded in transmission mode at the BM30 beamline[30] at the ESRF. At all stations, the energy of the incoming X-ray beam was calibrated by assigning the first inflection point of the transmission Fe K-edge X-ray absorption near-edge structure (XANES) recorded for a Fe foil to 7112.0 eV. Cl K-edge XAS data were recorded at the INE-Beamline [31] at the KIT Synchrotron Light Source (Karlsruhe, Germany) in fluorescence detection mode using a silicon drift detector. At this edge, the energy of the incoming X-ray beam was calibrated by assigning the maximum of the absorption edge recorded for KCl to 2822.8 eV. Several chlorine reference compounds were used, and solid compounds were stored in an oven at 40°C for at least 12 hours before measurements. Solutions were also prepared: 0.5 mol/L NaCl and an artificial cement porewater or ACW (5.9 mmol/L Na^+, 3.8 mmol/L K^+, 3.6 mmol/L Ca^{2+}, 2.8 µmol/L CO_3^{2-}, 5.8 mmol/L SO_4^{2-} and 3.8 mmol/l Cl^-,pH = 11). XAS data were treated following standard procedures using the Athena interface to the Ifeffit software [32].

For the analysis of pore water pH and chemical composition, the *ex-situ* leaching method described by Alonso et al.[33] was used. The evolution of the hydration process was monitored via pH and chemical composition analysis as a function of hydration time.

3.2 Leaching studies of the micro-mortar

Dissolution studies of micro-mortar were performed with two alternative methods. In first method (batch method), micro-mortar sample was submerged in groundwater at a solid/liquid ratio of 1 at the age of 28 days. pH of the liquid phase was determined according to Table 10. The experiments were performed in triplicate. In the second method (solution method), samples were sealed in plastic tubes in various temperatures. Detailed description of solution method is available elsewhere [34].

The experimental set-up used to study the alteration of the micro-mortar with bentonite water was performed to fully saturated samples. Samples were sealed with an epoxy resin, except for the exposed surface. The samples were exposed to bentonite-water (Table 3) for 6 months in a controlled argon atmosphere at room temperature. After exposure, the micro-mortar samples were immersed in isopropanol to displace the water and stop further reactions. The alteration zone was characterised by cutting the sample parallel to the flow direction and identifying the chemical perturbation using SEM-EDX. Additionally, after 6 months, the bentonite water was analysed for its concentration of cations and anions by inductively coupled plasma optical emission spectrometry (ICP-OES), inductively coupled plasma mass spectrometry (ICP-MS) and ion chromatography (IC).

3.3 Characterization of the concrete

Slump, air content, compressive strength and density were measured according to SFS-EN standards (SFS-EN 12350-2, SFS-EN 12350-7, EN 12390-3 and EN12390-9).

The chemical composition and structural properties were determined after 5 and 15 months, using XRD, thermogravimetry / differential thermal analysis (TG/DTA), SEM-EDX. XRD tests were completed on enriched powder samples in cement paste removing the coarse aggregates. Pore solution pH and composition were determined according to [33]. In addition, information on iron and chlorine speciation was obtained in the

same way described in section 3.1 for the micro-mortar and by probing their K-edge by XAS. Porosity was measured using the techniques described in section 3.5.

The diffusion coefficient was analysed using chloride migration transport according to NT Build 492 standard at the age of 18 months. Apparent diffusion coefficient (D_{app}) according to EN 12390-11 was determined at the age of 6, 9 and 12 months.

3.4 Percolation experiments with the concrete

A constant water pressure of 8 bars, was maintained to percolate groundwaters through the concrete samples. The percolated water composition and pH were monitored during the test, including the volume of the effluent flux to obtain the hydraulic conductivity. Additionally, at the end of each percolation test, the chemical, mineralogical and microstructural alterations in concrete were analysed at several distances from the groundwater inlet using XRD, TG/DTA and SEM.

3.5 Porosity and density measurements

Mercury intrusion porosimetry (MIP) - Intrusion and extrusion curves were obtained using Micromeritics Autopore IV 9500 volumetric set up on blocks of 2 cm^3 from atmospheric pressure up to 200.10^6 Pa. All the samples were heated under vacuum at 100°C for at least 36 hours and cooled under vacuum. Cumulative pore throat size distribution, up to the critical pore diameter, was calculated from the intrusion curve based on Washburn's law and a contact angle of 141.3°[35] , assuming a cylindrical pore shape. The bulk density (ρ) of each sample was also obtained before the first pressure step (3.10^3 Pa) The total intrusion porosity φMIP is also estimated from the maximum intruded specific volume of mercury V (intr.max) [m^3/kg] and ρ, [kg/m^3] using the following Equation 1.

$$\varphi(MIP) = V\,(intr.max) \times \rho \quad \text{(Equation 1.)}$$

Grain density was measured by helium pycnometry using a micromeretics accupyc 2020. Prior to measurement, the sample were dried at 100°C under vacuum for at least 36 hours.

Kerosene porosimetry - Total bulk porosity and grain density were measured by kerosene porosity method [36] and calculated from measured grain density (ρ_{gr}) (helium pycnometry) and apparent dry density (ρ) (mercury intrusion porosimetry) according to the following Equation 2.

$$\varphi = 1 - (\rho/\rho_{gr}) \quad \text{(Equation 2.)}$$

4. RESULTS AND DISCUSSION

4.1 Fresh-stage properties

Fresh stage properties of the concrete and the micro-mortar were measured after batching. The slump of the concrete was 180 mm, corresponding to typical easily workable concrete. The Haegermann flow of the micro-mortar was 200 mm, indicating easy-to-use mortar without risk of segregation. The fresh density of the concrete was 2420 kg/m^3 and 2110 kg/m^3 for the micro-mortar. The measured air content for the concrete was 1.0%.

4.2 Mechanical properties

The compressive strength evolution of concrete and micro-mortar are presented in Table 4. At the age of 7 days, the compressive strength of the concrete was 46.9 MPa and 64 MPa for the micro-mortar. The compressive strength of the concrete was similar to high performance concrete yet the result for micro-mortar was higher than that of the concrete studied. The punch test method presented similar compressive strength values for micro-mortar. According to the punch test method, the compressive strength of the

micro-mortar was dependent on the superplasticizer (Table 5). A change in superplasticizer brand reduced compressive strength, and even a change in the plasticizer batch had an effect on the micro-mortar compressive strength. The superplasticizer had a central role in dispersing cement and supplementary cementitious materials to ensure good reactivity. High dispersion of fines also increased workability, and enabled good consolidation during sample manufacture. Therefore, even a small change in superplasticizer quality induced changes in compressive strength. The plasticizer dosages used greatly exceeded the manufacturer's recommendations, which likely caused or increased the effects observed.

Table 4. *Compressive strength and densities of the concrete and the micro-mortar.*

Sample:	**Concrete**		**Micro-mortar**						
Method:	**SFS-EN**		**SFS-EN**		**Punch test**				
Environment:	**20°C RH100%**		**20°C RH100%**		**Humid air, 10°C**	**Granitic III, 10°C**	**B75, 10°C**	**Granitic III, 95°C**	**B75, 95°C**
Age [d]	**Compressive strength [MPa]**	**Density [kg/m³]**	**Compressive strength [MPa]**	**Density [kg/m³]**	**Compressive strength [MPa]**				
7	46.9	2420	64	2110	-	-	-	-	-
14	-	-	-	-	67	-	-	-	-
28	80.3	2430	104	2150	76	-	-	-	-
64	-	-	-	-	82	-	-	-	-
275	-	-	-	-	113	132	122	146	132
424	88.7	2420	-	-	-	-	-	-	-
550	-	-	-	-	112	116	109	146	129
723	-	-	149	2140	-	-	-	-	-
728	115.7	2450	-	-	-	-	-	-	-

Table 5. *The effect of superplasticizer quality to compressive strength in punch test.*

	Punch test		
	Naphtalene used in the project	Naphtalene different batch	Naphtalene from alternative source
Age [d]	Compressive strength [MPa]		
7	-	58.98	38.27
14	74.90	67.25	46.81
28	85.55	76.30	60.51
42	92.47	-	69.54
56	-	-	78.84
63	102.51	81.16	74.60

The study on the interaction of micro-mortar samples (Table 4) under various conditions revealed significant hardening during the initial phase of 9 months with stabilisation during a further 9 months. This effect is most significant at higher temperatures (at 95°C). The reference environment (humid air, 10°C) provided samples with the lowest compressive punch strength. Contrary to this, bentonite in suspension (labelled as B75) seems important for rigidity evolution (Table 6). Bentonite suspension stabilised rigidity value slightly below the level of initial tests while the reference and non-bentonite environment caused a slow increase of rigidity during the testing period.

Table 6. *Punch test method stiffness.*

	Punch test				
	Humid air, 10°C	**Granitic III, 10°C**	**B75, 10°C**	**Granitic III, 95°C**	**B75, 95°C**
Age [d]	**Rigidity [kN/mm]**				
275	35.2	32.2	27.5	32.6	26.4
550	40.3	38.0	27.6	36.2	29.9

4.3 Microstructure and transport properties

Microstructural characterisation by SEM indicated a dense C-S-H phases and low permeability structure for both the concrete and micro-mortar samples. Additionally, a good aggregate-cement paste of interfacial transition zone (ITZ) for the concrete was observed. Non-reacted silica fume (with a characteristic spherical shape), quartz and feldspar were also observed with the same technique.

Total porosity was determined by applying mercury intrusion porosimetry (MIP), helium pycnometer and kerosene porosity method (Table 7). Mercury intrusion porosity for the hardened micro-mortar was 6.1%, and between 2.5-3.8% for concrete. The mean pore size measured with mercury intrusion porosimetry was 0.01 µm. The total porosity of the concrete was 12.5% and 24.3% for the micro-mortar, as presented in Table 7. Results of low mercury intrusion porosity with respect to total porosity indicated that most of the porosity was nanosized, and the structure of concrete and micro- mortar was dense.

Table 7*. Porosities of the concrete and the micro-mortar.*

Material	**MIP**		**He pycno.**	**Kerosene porosity**		**Calculated porosity**
	Bulk density (r) (g/cm³)	**MIP**	**Grain density**	**Bulk density (r) (g/cm³)**	**Total porosity**	**j = 1-(r/rgr) (%)**
Micro-mortar	1.88	6.1 %	2.48	1.83	26.2 %	24.3 %
Concrete	2.28	3.8 %	2.61	2.28	12.5 %	12.8 %

Apparent diffusion coefficients for concrete were $0.73*10^{-12}$ m^2/s, $0.12*10^{-12}$ m^2/s and $0.12*10^{-12}$ m^2/s at the age of 6, 9 and 12 months, respectively. Chloride migration coefficient was $0.056*10^{-12}$ m^2/s at the age of 18 months. Compared to traditional OPC, effective diffusion and migration coefficients were low. Hydraulic conductivity with 8 MPa water pressure was 10^{-13} m/s for the concrete.

4.4 Chemical properties

Pore solution pH evolution for concrete and micro-mortar is presented in Table 8. Elemental composition of concrete pore solution is presented in Table 9. The pH of studied solutions decreased over time due to proceeding pozzolanic reaction and C-S-H polymerization and all cases the pH is below that of a portlandite saturated solution (pH 12.5)

Table 8. *pH development of studied concrete and micro-mortar (temperature = 20°C)*

Temp.	**Concrete**	**Micro-mortar**
Age (days)	**pH**	
7	12.16	
19	11.94	
28	11.91	12.26
150	11.47	11.70
424	11.46	11.56
728	11.35	11.61

Table 9. *Elemental composition of concrete pore solution after 150 and 450 days.*

Water soluble ions [ppm]	***Concrete (150 d)***	***Concrete (450 d)***
Al	*0.70*	*0.01*
Ca	*50.87*	*20.82*
Fe	*0.14*	*0.00**
Mg	*0.58*	*1.45*
S	*111.19*	*90.20*
Si	*50.53*	*40.75*
Na	*101.17*	*115.25*
K	*52.01*	*39.93*

**Under detection limit.*

Full characterization of the micro-mortar was possible by using different complementary analytical techniques (XRD. TG-DSC, SEM-EDX, ^{29}Si and ^{27}Al MAS NMR, XAS), even identifying minor phases, relevant for radionuclide retention processes (Cl- and Fe-bearing phases). The same was true for the concrete, but in that case ^{29}Si and ^{27}Al MAS NMR were not used making the identification of minor Al-phases such as ettringite difficult. Quartz was identified by XRD as the main crystalline phase present in the solid. Calcium-silicate-hydrates (C-S-H) and calcium-aluminate-silicate-hydrates (C-A-S-H) were identified with ^{29}Si and ^{27}Al MAS. Furthermore, ettringite was identified as a minor phase with the same technique. TG/DTA presented a mass loss around 100-300°C which was attributed to C-S-H hases and ettringite[37]. However, in this temperature range the mass loss can also be attributed to water bound to mineral surfaces which were calculated for the micro-mortar (11%) according to the method described in [38], making a quantification of the C-S-H phases difficult. The weight loss at 450 °C, indicative for portlandite was not observed, in agreement with the measured pH (see Table 8). Additionally, the Ca/Si -ratio of the C-S-H phases were between 0.5-0.7 for both the concrete and the micro-mortar, with the and Al/Si-ratio around 0.05. The ^{29}Si MAS NMR spectrum is depicted in Figure 1. A broad signal in the chemical shift range between -75 and -100 ppm was the main signal of the spectrum and was assigned to the Si present in the C-S-Hphases The overlap of the signals did not allow unambiguous deconvolution but it is know that the spectra of C-S-H phases consists of at least three resonances called Q1, Q2(1Al) and Q2 [38], [39]. The main signal can also be overlapped with a minor signal of feldspar (-95 to -100 ppm). The signal at -69 ppm resulted from unreacted clinker (alite).. The broad feature at −110 ppm is characteristic of unreacted silica fume and quartz.

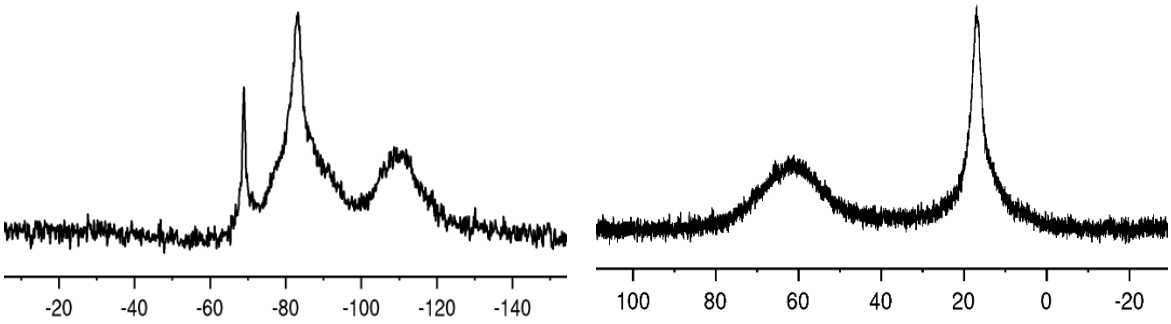

Figure 1: *^{29}Si MAS NMR spectra (left) and ^{27}Al MAS NMR spectra of the micro-mortar*

The ^{27}Al-NMR spectrum (Figure 1) presented two different signals at 63.0 and 16.7 ppm, indicating that Al was in both octahedral and tetrahedral coordinations[40]. The observed tetrahedrally coordinated ^{27}Al

resonances were associated with the aluminium in the bridging position of the C-S-H phases and feldspar, and the octahedral ^{27}Al with the presence of ettringite and probably some aluminium/iron substitution.

Information on Fe speciation was studied by probing the Fe K-edge by XAS. The XANES is particularly sensitive to the type and number of neighbouring elements as well as bond distances and geometrical arrangement. For all samples and reference compounds, the XANES exhibited a feature at around 7114.5 eV (Figure 2) that derived predominantly from $1s \rightarrow 3d$ transitions. In O_h symmetry, this transition is forbidden, whereas in T_d symmetry the $1s(a_1) \rightarrow t_2$ transition is allowed (e.g., Westre et al. [41]. Thus, no pre-edge feature should be observed for octahedrally coordinated Fe. However, very weak features were still observed, and the intensity depended on the local symmetry and electronic properties of the cation. The intensity of the pre-edge was therefore low for common octahedral sites (e.g., hematite, goethite) and substantial for tetrahedral sites. The pre-edge of the micro-mortar and the concrete were located at a position similar to reference compounds, which contained only ferric iron. Therefore, the micro-mortar and the cement contain ferric iron. Furthermore, the intensity of the pre-edge of the micro-mortar seemed slightly larger as in the concrete, implying that the former contained substantial amounts of tetrahedral Fe^{3+}, but the latter only marginal amounts.

Further information was obtained from the analysis of the main absorption edge. The XANES of the reference compounds C2F and C4AF were very similar with the presence of two shoulders on the high-energy side of the main absorption edge. This finding can be explained by the crystallization of both compounds in the same crystal system (orthorhombic). Interestingly, the XANES of the clinker also bore similarities with that of C2F and C4AF, pointing to the presence of these compounds or at least one of them in the clinker. Similarly, the XANES of both C-S-H phases bore similarities, only the intensity of the shoulder after the main absorption edge slightly differed. The XANES of the micro-mortar differed from the concrete, implying the location of Fe in different chemical environments. The XANES of the former contained a shoulder, whereas the XANES of the second is rather sharp. A closer inspection of the absorption edge of the micro-mortar suggests similarities with that of C2F or C4AF, and also with that of the C-S-H calcium-silicate-hydrate phases. These results agreed with the observed intensity of the respective pre-edge features. The presence of minor amounts of other compounds was impossible to exclude. The XANES of the concrete significantly differed from that of most reference compounds. Though the XANES of ferrihydrite did not contained any shoulder, it differed from that of the concrete, which did not exclude the presence of low amounts of this reference compound in the sample.

Extended X-ray absorption fine structure (EXAFS) spectra of C2F and C4AF were very similar and observed differences in terms of oscillation amplitudes, was attributed to replacement of a fraction of Fe by Al within the structure. Though noisier, the spectrum of the clinker also was similar to that of these reference compounds. Likewise, the spectra of the C-S-H had similarities, suggesting closely related binding environments. Other important information was derived from comparison of the spectra. The spectra of C2F, C4AF and the clinker had a first oscillation around 4.1 $Å^{-1}$, like most reference compounds, and a second oscillation or shoulder at ~4.8 $Å^{-1}$, in contrast to the other reference compounds. The presence of this second frequency was attributed to the presence of tetrahedral iron, which agreed with the structures of C2F and C4AF [42]. Recently reported EXAFS spectra for ferric saponite, a smectite containing Fe^{3+} at tetrahedral position, exhibit oscillations at similar positions [43], thus strengthening the attribution of this spectral feature to tetrahedral ferric iron. The EXAFS spectrum of the micro-mortar mainly differed from that of the concrete in the spectral features in the 4 – 6 $Å^{-1}$ range. Still, both had an oscillation amplitude maximum at ~4.1 $Å^{-1}$, implying the presence of octahedral Fe^{3+}. The spectrum of the micro-mortar had a shoulder at ~4.7 $Å^{-1}$ which was absent in the spectrum of the cement, whereas the spectrum of the cement had a feature at ~5.2 $Å^{-1}$ which was absent in the spectrum of the micro-mortar. By comparison with reference compounds, only spectra of C2F, C4AF and the clinker had a shoulder at k ~4.8 $Å^{-1}$, signifying that at least a fraction of Fe

in the micro-mortar was located in an environment similar to that of these reference compounds. Interestingly, this result also agreed with the shoulder at k ~7 $Å^{-1}$ in the spectrum of the micro-mortar, because all other reference compounds had an oscillation amplitude minimum at this k value. Results pointed to the presence of Fe in various environments in the sample. Unfortunately, the spectrum of the cement differed from that of the reference compounds. Hints of the presence of octahedral Fe^{3+}, probably in substantial amounts was also observed. EXAFS data corroborated conclusions obtained by analysis of the XANES.

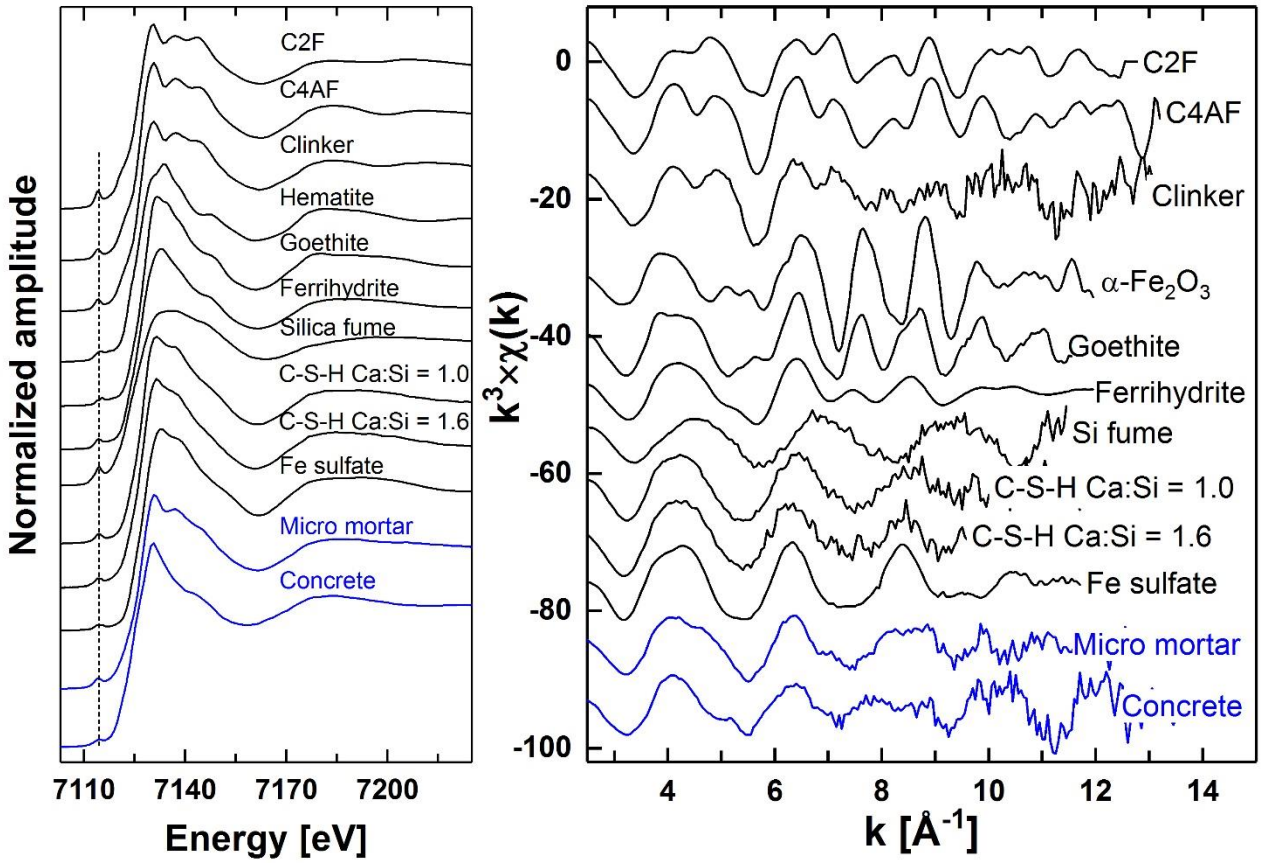

Figure 2: *Fe K-edge XANES (left) and EXAFS spectra (right) of the micro-mortar, the concrete and the reference compounds. The vertical dashed line in the XANES indicates the position of the pre-edge features.*

For chlorine, only Cl K-edge XANES were recorded for the micro-mortar, the concrete and reference compounds (Figure 3). The XANES of the liquid reference compounds differed significantly from that of all solid compounds. For the solid compounds, the maximum of the main absorption edge was located at similar energy position, implying that all compounds contained chloride ions. Friedel's and Kuzel's salt have very similar XANES with a shoulder at ~2827 eV, hinting at comparable environments. The XANES of both C-S-H phases differed: the XANES of the phase with higher Ca content had a weak shoulder at ~2827 eV, whereas the XANES of the phase with higher Si content exhibited a distinctive feature at ~2833 eV. The XANES of the sodium, calcium and potassium chloride differed from each other, in agreement with differences in their crystal structures. XANES of the micro-mortar and the concrete were very similar. This result hinted at comparable Cl environments in the samples, and excluded the presence of significant amounts of reference compounds such as C-S-H phases, Kuzel's and Friedel's salts, NaCl and KCl. The XANES of $CaCl_2.2H_2O$ bore similarities with the samples, however the absorption edge was wider and higher in amplitude. Additional reference compounds would be needed to identify the Cl binding environment in the micro-mortar and in the cement.

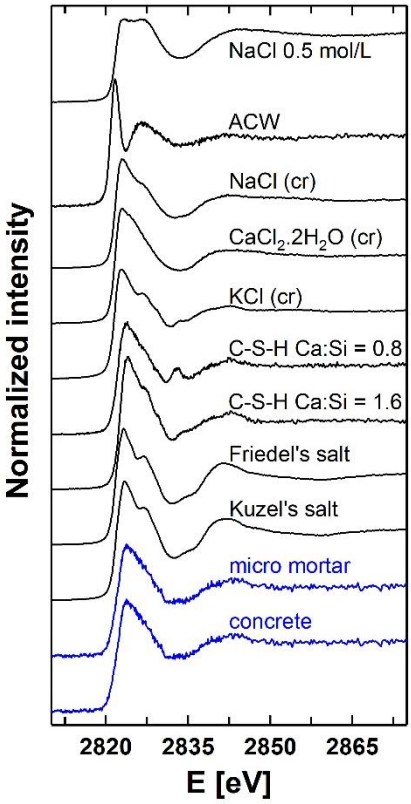

Figure 3: *Cl K-edge XANES of the micro-mortar, the cement and reference compounds.*

4.5 Leaching and percolation experiments

Leaching and percolation experiments were performed on concrete and micro-mortar samples according to the procedure described in sections 3.2 and 3.4. Results are presented in Table 10. According to Table 10, groundwater and sample composition had an effect on measured pH values. Concrete samples had lower pH values than micro-mortar samples, although rigorous convolution is not possible. Temperature also had a clear effect on pH development. In a 10°C environment, the pH decrease was very slow compared to 20°C.

Table 10. *pH development of studied concrete and micro-mortar in various temperatures, groundwater exposures and measurement set-ups.*

Temp.	20°C	20°C	20°C	20°C	20°C	10°C	95°C	
Solution	Granitic I	Granitic II	Clay I	Clay II	Saline	Granitic III	Granitic III	B75
Method	Batch	Percolation	Batch	Percolation	Batch	Solution pH	Solution pH	Solution pH
Sample	Micro-mortar	Low-density concrete	Micro-mortar	Low-density concrete	Micro-mortar	Micro-mortar	Micro-mortar	Micro-mortar
Age	pH							
29	11.33		10.67		11.02			
30	11.42		10.89		11.15			
31	11.47		11.11		11.24			
32	11.35		11.05		11.14			
33	11.44		11.13		11.2			
37	11.37		11.21		11.29			
45						11.96	11.96	11.96
58	11.13		10.93		10.87			
88	10.81		10.54		10.66			
120	10.64		10.48		10.74			
155	10.46		10.23		10.56			
175						12.31	11.02	
180	10.39		10.21		10.51			
210		8.8 (45ml)*		8.2 (150ml)*				
211	10.38		10.24		10.39			
265	10.52		10.17		10.55			
322						11.87	10.8	10.85
329	10.68		10.14		10.64			
330		8.5 (35ml)*		7.7-8.2 (175ml)*				
394	10.73		10.25		10.47			
450		9.0 (75ml)*		8.1-8.3 (40ml)*				
455						11.75	11.57	
567						11.48	10.8	10.67

**Volume of the percolated solution.*

4.6 Influence of leaching on microstructure and chemical composition

Figure 4 shows a cross-section by SEM-EDX of micro-mortar after contact with bentonite solution during 180 days at room temperature and anoxic condition. Note that the crack observed in the figure was produced during the cutting of the sample after the degradation experiments. Additionally, hollow shell pores having sizes in the range of about 1-15 µm were also identified. These pores were embedded in cement gel and appeared to be connected to the continuous capillary pore system by much smaller gel pores. From the images it can be clearly seen that the sample had an initial heterogeneous mineralogical composition. (in the studied spatial scale), identifying calcium-(aluminate)-silicate-hydrate phases, blast furnace slag, quartz filler and initial clinker (belite, ferrite). Furthermore, a reacting front at 400 µm from the surface in contact with

the bentonite water was clearly distinguished. Chemical composition of the bentonite solution after 6 months of exposure is presented in Table 11.

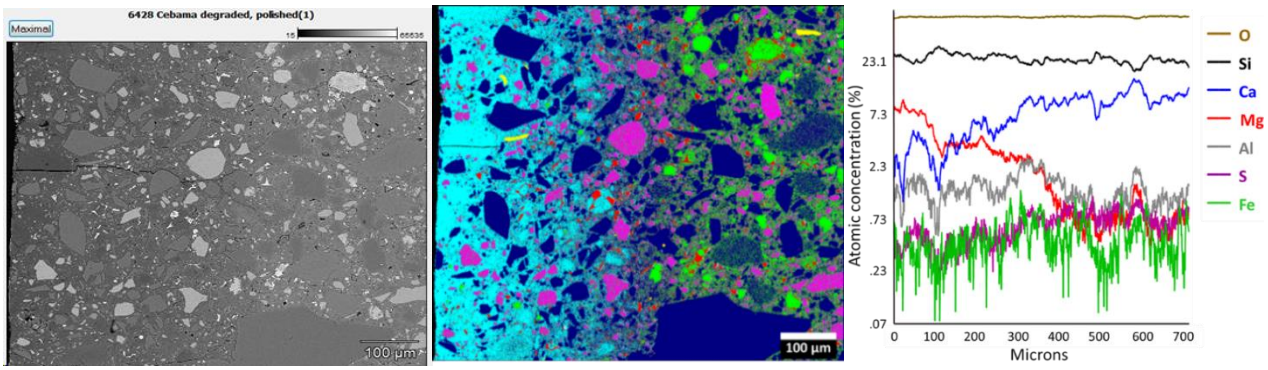

Figure 4: *Cross-section of micro-mortar after contact with bentonite pore water by SEM-EDX. Phase distributions in false colours (centre) overlaying the backscattered electron image presenting a material contrast of micro-mortar (left). Left side at images: surface of cement. Mg-exchanged C-S-H (cyan, C/S=0.17), quartz filler (blue), $MgAlCa_4Si_3O_xH_y$ (pink), belite (green), tetracalcium aluminoferrite (red), muscovite (yellow). Note that the crack observed in the figure was produced during the cutting of the sample after the degradation experiments. Elemental depth profile extracted from SEM-EDX map data (right).*

Table 11. *Chemical composition of Bentonite -solution after 6 months in contact with the micro-mortar. Initial composition is presented in Table 3.*

mg/L	***pH***	***Si***	***Mg***	***Na***	***K***	***Ca***	***Cl***	***SO_4^-***	***Al***
	10.07	*12.02*	*1.44*	*3832*	*167*	*412*	*627*	*8783*	*1.46*

In order to identify the chemical processes occurring in that area, the cross section was analysed (homogenised 700 µm) giving the elemental depth profile depicted in Figure 4. Due to the high gradient in Mg concentration between the bentonite water and the cement solid, magnesium diffused into the solid sample and started to exchange with the calcium present in the calcium-(aluminate)-silicate-hydrate phases. Magnesium concentration close to the surface was three times higher than calcium suggesting the formation of magnesium-silicate-hydrate phases by decalcification of the C-S-H phases. This would agree with the observed decreasing atomic ratio with the distance, and at 140 µm the Mg/Ca -ratios were equal. Finally, at 400 µm the Ca/Mg-ratio keeps constant and equal to the initial ratio, suggesting that the reactive front during 6 months was 400 µm. Other cation exchange with calcium was Na which was present initially in high concentration (~ 0.25M) in the bentonite water and decreased after 6 month interaction. In addition, the elemental depth profile showed a decrease of sulphate in the altered zone.

Apart from these main processes, it seems also obvious that the clinker (belite and ferrite) was hydrating/reacting in the magnesium exchanged zone with the aqueous solution to form magnesium containing phases (i.e. Mg-exchanged C-S-H phases). It can be seen that the blast furnace slag and the quartz filler remained in the samples as non-reactive solids or presenting a slow kinetic dissolution. Finally, precipitation of calcite had only been observed on the holes present in the surface in contact with the bentonite water and not in the pore structure.

A clear reaction front was also observed in samples in the percolation experiments with granitic I, saline and clay I -groundwater (Figure 5). In the reaction front, calcium content was depleted compared to non-affected internal parts of the samples. In groundwater compositions containing substantial magnesium concentrations, a magnesium enrichment was observed in the reaction front. Calcium salt precipitation was

observed at the surface of the sample in saline groundwater. It is likely that the formation of calcium precipitate decreased the rate magnesium penetration into the sample, as a difference between clay- and saline groundwater was observed. In clay groundwater, the magnesium penetration was stronger compared to saline groundwater.

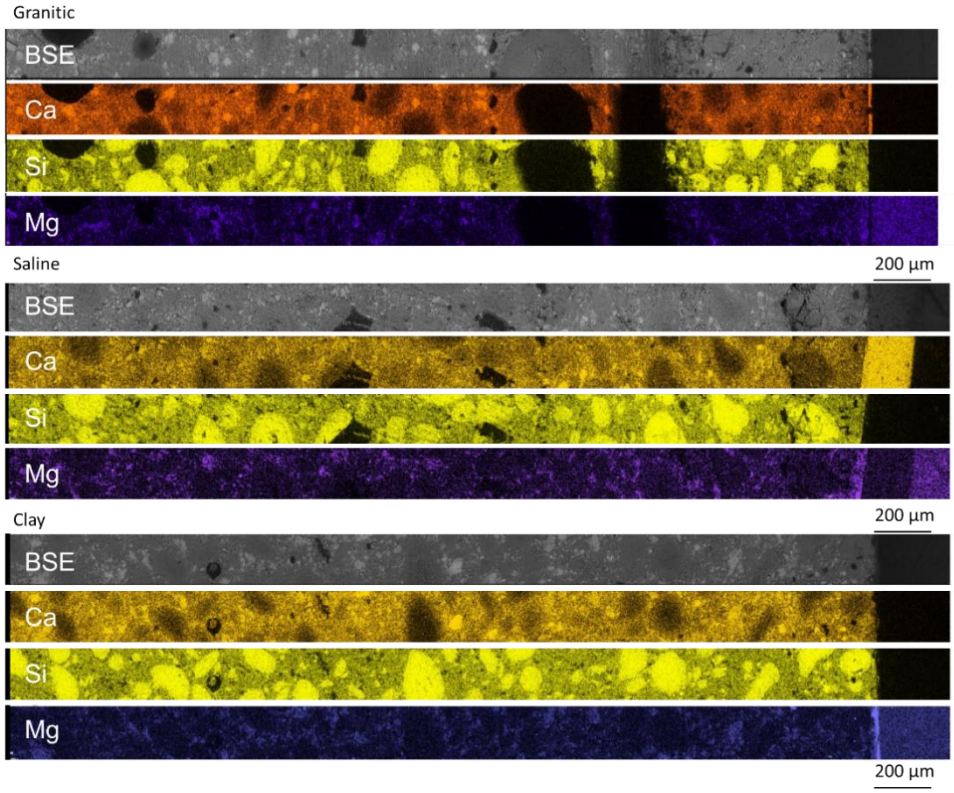

Figure 5: *Scanning elemental maps of Ca, Si and Mg in micro-mortars exposed to Granitic I, Saline and Clay I -groundwater.*

For micro-mortar samples in direct contact with bentonite slurry (B75), a calcium enrichment was observed in bentonite in the vicinity of the sample surface (Figure 5). Within studied groundwater compositions and timescales, other major changes were not identified.

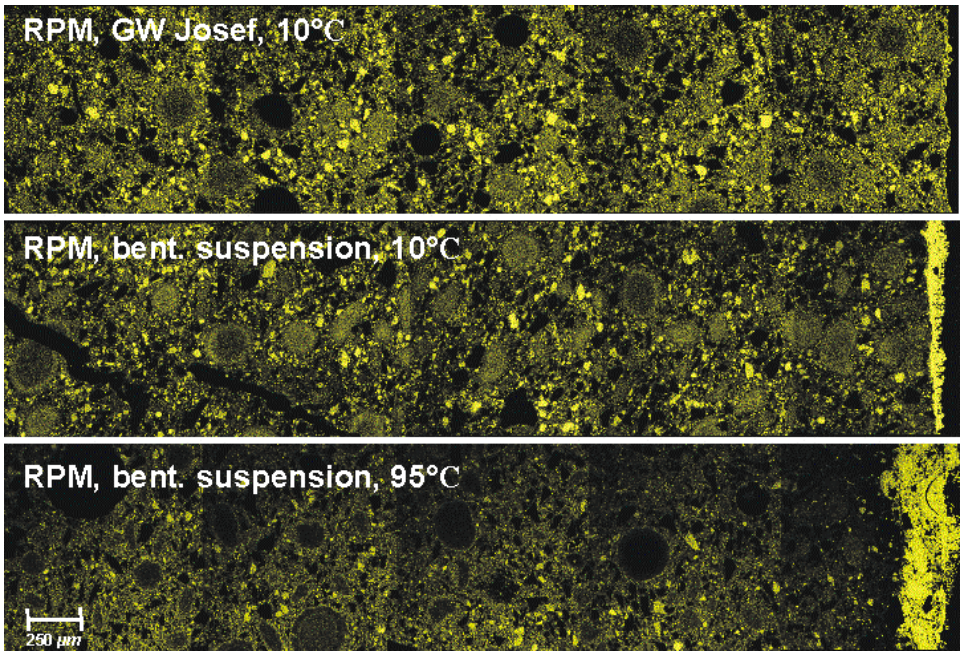

Figure 6: *Scanning electron images with Ca elemental map (yellow) showing the calcium enrichment at the interaction boundary with bentonite suspension (B75).*

5. CONLUSIONS

The properties of the concrete and the micro-mortar were not identical, but similar, especially regarding mechanical properties. Chemical properties of the concrete and micro-mortar differed slightly due to the lower water content used in the micro-mortar. When evaluating low pH material performance, it was concluded that the essential properties of slag-based mix designs did not differ from fly ash and silica fume based mix designs. The pore solution pH and pH development were comparable to fly ash and silica fume based mix designs. Compressive strengths were also similar. Leachate compositions did not differ significantly from fly ash or silica fume mix designs. On the basis of these results, it can be deduced that slag is able to replace fly ash when producing ternary ”low-pH” mixtures in the future, if needed due to material supply or quality problems.

The compressive strengths of the concrete and micro-mortar were very high and comparable to high performance concretes. Microstructural analyses and effective diffusion coefficients showed dense and homogeneous microstructures. Effective diffusion coefficients were ten times lower than traditional concrete. Total porosity of the concrete mainly consisted of nanoscale porosity. The total volume of porosity was also low compared to ordinary Portland cement-based concretes. The results clearly show that the performance of “low-pH” mix designs exceeds the performance of traditional Portland cement concretes and are comparable to high performance concretes. ”Low-pH” mix designs are thus very suitable construction materials, if the mix design is performed accordingly and the mixing methodology and emplacement method results in a homogeneous mix.

Chemical characterisation of the micro-mortar identified ettringite, which was not identified in the concrete. The observation further supports the anticipated lower reactivity of the micro-mortar compared to the concrete samples. According to the pH measurements, the pore solution pH of the micro-mortar was below the saturation pH of portlandite.

XAS analysis provided information on Fe and Cl speciation in the micro-mortar and in the concrete. The data suggest that the Fe environment in the micro-mortar differed from that in the cement, and that Fe was present only as ferric iron in both materials. In the micro-mortar, Fe was present at both tetrahedral and octahedral sites. Binding environments may be similar to that in C2F or C4AF, and possibly C-S-H phases. In the cement, data suggest that Fe predominated at octahedral sites. Upcoming modelling of EXAFS data will provide additional information in terms of the nature and numbers of neighbouring atoms and bond distances. XAS pointed to a similar binding environment for Cl in the micro-mortar and cement, and ruled out the presence of Cl in an environment comparable to that in the liquid phase. Data also excluded the presence of Cl in an environment comparable to that in Kuzel's or Friedel's Salt and C-S-H phases. The use of additional reference compounds would be needed to obtain information on Cl speciation.

A deep alteration zone was observed within relatively short exposure times compared to the lifetime of a repository. In contact with magnesium containing groundwater, cation exchange took place between the concrete studied and groundwater. Calcium depletion and magnesium enrichment at the reaction front is not a unique quality of slag-based "low-pH" mix designs. Similar reaction front has been observed also in fly ash and silica fume based "low-pH" mix designs. Magnesium increase and calcium depletion were observed in alteration zones. Where bentonite was in contact with the samples, calcium enrichment was observed in the bentonite. The effect of cation exchange on the most important qualities of bentonite, e.g. swelling potential, should be studied further, as these changes are kinetically possible during the lifetime of the repository.

The extent of the reaction front in the sample should be noticed. The alteration depth was 400 µm from the surface, within an exposure period of 180 days under anoxic condition. An exposure period of 180 days is very short compared to the lifetime of the repository which extends over several hundred thousands of years. The role of cation exchange on interface and bentonite properties should be clarified to ensure that the presence of cementitious materials does not endanger the functionality of the engineered barrier.

The results of this study are being utilised by waste management organisations to develop material specifications and their performance to be used in the safe isolation of HLW in underground repositories.

ACKNOWLEDGEMENTS

The research leading to these results has received funding from the European Union's European Atomic Energy Community's (Euratom) Horizon 2020 Programme (NFRP-2014/2015) under grant agreement, 662147 - "Cebama". Additionally, KIT-INE acknowledges the ESRF and the KIT Synchrotron Light Source for provision of synchrotron radiation beam time and D. Banerjee for assistance during measurements at the BM26A beamline. We thank B. Lothenbach (EMPA, Switzerland) and S. Grangeon (BRGM, France) for providing reference compounds for the XAS study. The authors also acknowledge the support provided by many supervisors and technical experts during the course of this work: Nicolas Finck, Dieter Schild, Thorsten Schäfer, Christian Adam, Kathy Dardenne and Jörg Rothe from KIT; A. Fernandez and J.L. Garcia-Calvo from CSIC; M. Felipe-Sotelo and M. Isaacs from University of Surrey; Tomáš Rosendorf from ÚJV Řež, a. s.; John Provis and Neil Hyatt from University of Sheffield; Mia Löija and Hanna Iitti from VTT.

REFERENCES

[1] World Nuclear Association, registered in England and Wales and U. K. Registered office: Tower House, 10 Southampton Street, London, WC2E 7HA, "Radioactive waste Management." [Online]. Available: http://www.world-nuclear.org/information-library/nuclear-fuel-cycle/nuclear-wastes/radioactive-waste-management.aspx. [Accessed: 28-Jun-2019].

[2] "General Time Schedule for Final Disposal," *Posiva Oy Olkiluoto, 27160 Eurajoki.* .

[3] "Timetable," *Nagra*. [Online]. Available: https://www.nagra.ch/en/timetable.htm#. [Accessed: 28-Jun-2019].

[4] J. Palomaeki and L. Ristimaeki, "Facility Description 2012. Summary report of the encapsulation plant and disposal facility designs." 2013.

[5] K. Koskinen, "Effects of Cementitious Leachates on the EBS," *Posiva Oy*, vol. 31, no. January, 2014.

[6] C. Cau Dit Coumes, S. Courtois, D. Nectoux, S. Leclercq, and X. Bourbon, "Formulating a low-alkalinity, high-resistance and low-heat concrete for radioactive waste repositories," *Cem. Concr. Res.*, vol. 36, no. 12, pp. 2152–2163, 2006.

[7] E. Holt, M. Leivo, and T. Vehmas, "Low-Ph Concrete Developed for Tunnel End Plugs Used in," 2014.

[8] T. T. H. Bach, "Physico-chemical evolution of low-pH cements : influence of the temperature and the retention mechanisme of alkalins," Université de Bourgogne, 2010.

[9] J. L. Garcia, M. C. Alonso, A. Hidalgo, and L. F. Luco, "Design of low-pH cementitious materials based on functional requirements," in *Proc. R&D on Low-pH Cement for a Geological Repository, 3rd Workshop, June*, 2007, pp. 13–14.

[10] J. L. Garcia Calvo, A. Hidalgo, C. Alonso, and L. Fernandez Luco, "Development of low-pH cementitious materials for HLRW repositories. Resistance against ground waters aggression," *Cem. Concr. Res.*, vol. 40, no. 8, pp. 1290–1297, 2010.

[11] J. B. Martino, "Low heat high performance concrete used in a full-scale tunnel seal," in *Proceeding 3rd workshop R&D on low pH cement for a geological repository, Paris, June*, 2007, pp. 13–14.

[12] M. Codina, C. Cau-dit-Coumes, P. Le Bescop, J. Verdier, and J. P. Ollivier, "Design and characterization of low-heat and low-alkalinity cements," *Cem. Concr. Res.*, vol. 38, no. 4, pp. 437–448, Apr. 2008.

[13] T. Nishiuchi, T. Yamamoto, M. Hironaga, and H. Ueda, "Mechanical properties of low pH concretes, LAC, HFSC AND SAC," in *Proceeding 3rd workshop R&D on low pH cement for a geological repository, Paris, June*, 2007, pp. 13–14.

[14] B. Lothenbach, E. Wieland, B. Schwyn, R. Figi, and D. Rentsch, "Hydration of low-pH cements.," in *International workshop on the mechanisms and modelling of cement / waste Interactions,*.

[15] L. R. Dole and C. H. Mattus, "Low pH concrete for use in the US high-level waste repository: Part I overview," in *Proceeding 2nd workshop R&D on low pH cement for a geological repository, Madrid, Spain, June*, 2007, pp. 15–16.

[16] A. Dauzères *et al.*, "On the physico-chemical evolution of low-pH and CEM I cement pastes interacting with Callovo-Oxfordian pore water under its in situ CO2 partial pressure," *Cem. Concr. Res.*, vol. 58, pp. 76–88, Apr. 2014.

[17] E. Holt, M. Leivo, and T. Vehmas, "Low-pH concrete developed for tunnel end plugs used in nuclear waste containment," in *concrete Innovation Conference (CIC2014)*, 2014.

[18] E. Holt and P. Koho, "POPLU Experimental summary report," DOPAS project, Deliverable D4.5, 2016.

[19] H. F. W. Taylor, *Cement Chemistry*, 2nd ed. London: Thomas Telford Publishing, Thomas Telford Services Ltd, 1997.

[20] M. Leivo, T. Vehmas, and E. Holt, "Developing Low pH concrete for tunnel plugging structures in nuclear waste containment," in *XIII Nordic Concrete Research Symposium - Reykjavik, Iceland Duration: 13 Aug 2014 → 15 Aug 2014*, 2014, pp. 491–494.

[21] “Cement based materials, properties, evolution, barrier functions (CEBAMA).” [Online]. Available: www.cebama.eu. [Accessed: 28-Jun-2019].

[22] A. Idiart *et al.*, “Benchmark of reactive transport models within Cebama: Application to a concrete/clay interface,” *Appl. Geochemistry*, p. submitted, 2019.

[23] T. Vehmas, A. Schnidler, M. Löija, M. Leivo, and E. Holt, “Reference mix design and castings for low-pH concrete for nuclear waste repositories,” *Horiz. 2020 CEBAMA Proj.*, p. 101, 2017.

[24] E. Holt, F. Claret, and U. Mäder, “Report on WP1 selected experimental materials to be used, including both new laboratory and aged in-situ samples,” CEBAMA Deliverable D1.05, 2016.

[25] M. H. Bradbury and B. Baeyens, “Physico-chemical characterisation data and sorption measurements of Cs, Ni, Eu, Th, U, Cl, I and Se on MX-80 bentonite,” Switzerland, 2011.

[26] Český geologický ústav (Czech Geological Institute), “Metodiky laboratorních zkoušek v mechanice zemin a hornin (Methods of laboratory testing in soil and rock mechanics),” Prague, 1987.

[27] P. Večernik *et al.*, “Interaction between cement and Czech bentonite under temperature load and in in-situ conditions: an overview of experimental program,” *Horiz. 2020 CEBAMA Proj.*, p. 77, 2016.

[28] R. Vašíček, R. Červinka, V. P, R. T, and S. J, “Geochemical and Thermal Impacts on the Characteristics of Cementitious Materials: Strength, Leachate pH, Mineralogy And Diffusion,” in *Third Annual Workshop of the HORIZON 2020 CEBAMA Project*, 2018.

[29] S. Nikitenko *et al.*, “Implementation of a combined SAXS/WAXS/QEXAFS set-up for time-resolved in-situ experiments,” *J. Synchrotron Radiat.*, vol. 15, no. 6, pp. 632–640, 2008.

[30] O. Proux *et al.*, “Feedback system of a liquid-nitrogen-cooled double-crystal monochromator: design and performances,” *J. Synchrotron Radiat.*, vol. 13, no. 1, pp. 59–68, 2006.

[31] J. Rothe *et al.*, “The INE-Beamline for actinide science at ANKA,” *Rev. Sci. Instrum.*, vol. 83, no. 4, p. 043105, Apr. 2012.

[32] B. Ravel and M. Newville, "data analysis for X-ray absorption spectroscopy using IFEFFIT,” *J. Synchrotron Radiat.*, vol. 12, no. 4, pp. 537–541, 2005.

[33] M. C. Alonso, J. L. Garcia Calvo, and C. Walker, “Development of an accurate pH measurement methodology for the pore fluids of low pH cementitious materials,” Sweden, 2012.

[34] R. Vašiček, P. Večernik, J. Hloušek, R. Červinka, L. Hausmannová, and V. Havlová, “Interaction between cement and Czech bentonite under temperature load and in in-situ conditions: results after first testing period,” in *Proceedings of the Second Workshop of the HORIZON 2020 CEBAMA Project (KIT Scientific Reports; 7752)*, 2019, vol. 7752, p. 93.

[35] E. W. Washburn, “The dynamics of capillary flow,” *Phys. Rev.*, vol. 17, no. 3, p. 273, 1921.

[36] S. Gaboreau, D. Prêt, E. Tinseau, F. Claret, D. Pellegrini, and D. Stammose, “15 years of in situ cement–argillite interaction from Tournemire URL: Characterisation of the multi-scale spatial heterogeneities of pore space evolution,” *Appl. Geochemistry*, vol. 26, no. 12, pp. 2159–2171, 2011.

[37] K. Scrivener, R. Snellings, and B. Lothenbach, *A practical guide to microstructural analysis of cementitious materials*. Crc Press, 2018.

[38] B. Lothenbach, G. Le Saout, M. Ben Haha, R. Figi, and E. Wieland, “Hydration of a low-alkali CEM III/B–SiO2 cement (LAC),” *Cem. Concr. Res.*, vol. 42, no. 2, pp. 410–423, Feb. 2012.

[39] I. Richardson, “The nature of C-S-H in hardened cements,” *Cem. Concr. Res.*, vol. 29, no. 8, pp. 1131–1147, Aug. 1999.

[40] E. L'Hôpital, B. Lothenbach, D. A. Kulik, and K. Scrivener, "Influence of calcium to silica ratio on aluminium uptake in calcium silicate hydrate," *Cem. Concr. Res.*, vol. 85, pp. 111–121, Jul. 2016.

[41] T. E. Westre, P. Kennepohl, J. G. DeWitt, B. Hedman, K. O. Hodgson, and E. I. Solomon, "A Multiplet Analysis of Fe K-Edge 1s → 3d Pre-Edge Features of Iron Complexes," *J. Am. Chem. Soc.*, vol. 119, no. 27, pp. 6297–6314, 1997.

[42] A. A. Colville and S. Geller, "The crystal structure of brownmillerite, Ca${\sb 2}$FeAlO${\sb 5}$," *Acta Crystallogr. Sect. B*, vol. 27, no. 12, pp. 2311–2315, 1971.

[43] N. Finck *et al.*, "Structural iron in smectites with different charge locations," *Phys. Chem. Miner.*, vol. 46, no. 7, pp. 639–661, 2019.